Nanosize Storage Properties in Spinel $Li_4Ti_5O_{12}$ Explained by Anisotropic Surface Lithium Insertion

Swapna Ganapathy and Marnix Wagemaker*

Fundamental Aspects of Materials and Energy, Department of Radiation, Radionuclides and Reactors, Faculty of Applied Sciences, Delft University of Technology, Mekelweg 15, 2629 JB Delft, The Netherlands

ABSTRACT Nanosizing is a frequently applied strategy in recent years to improve storage properties of Li-ion electrodes and facilitate novel storage mechanisms. Due to particle size reduction, surface effects increasingly dominate, which can drastically change the storage properties. Using density functional theory calculations we investigate the impact of the surface environment on the Li-ion insertion properties in defective spinel $Li_{4+x}Ti_5O_{12}$, a highly promising negative electrode material. The calculations reveal that the storage properties strongly depend on the surface orientation. The lowest energy (1 1 0) surface is predicted to be energetically favorable for Li-ion insertion into the vacant *16c* sites. The (1 1 1) surface allows capacities that significantly exceed the bulk capacity $Li_7Ti_5O_{12}$ at voltages greater than 0 V by occupation of *8a* sites in addition to the fully occupied *16c* sites. One of the key findings is that the surface environment extends nanometers into the storage material, leading to a distribution of voltages responsible for the curved voltage profile commonly observed in nanosized insertion electrode materials. Both the calculated surface-specific voltage profiles and the calculated particle size dependent voltage profiles are in good agreement with the experimental voltage profiles reported in literature. These results give a unique insight into the impact of nanostructuring and further possibilities of tailoring the Li-ion voltage profiles and capacities in lithium insertion materials.

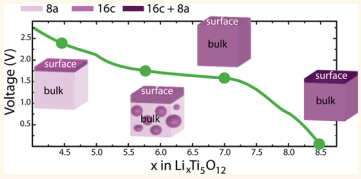

KEYWORDS: Li-ion battery · nanosize effects · spinel $Li_{4+x}Ti_5O_{12}$ · Li surface storage · density functional theory

Considerable research has been focused on the nanosizing of electrode materials for Li-ion batteries. Nanomaterials offer several possibilities to improve Li-ion battery performance. Shorter Li-ion diffusion and electronic conduction pathways offer potentially higher (dis)charge rates, and the nanodimensions allow reactions that appeared impossible at the microscale.[1,2] The altered voltage profiles indicate that nanosizing also has a large impact on the thermodynamics of Li-ion insertion reactions. The first-order phase transition upon (dis)charge leads in many insertion materials to a constant voltage profile. Nanosizing these materials results in a curved open cell voltage profile with a much smaller plateau region in comparison with micrometer sizes of the same material. This may indicate a reduced miscibility gap, which has been attributed to strain,[3] the diffusion interface,[4,5] and contributions from the interface and surface energies that arise during Li-ion insertion.[6] It has been shown that the curved voltage profile may also arise in part due to surface energies and the particle size distribution[7] inherently present in nanosized materials. More recently it has been demonstrated that the entropy of discrete filling of individual particles leads to a curved voltage profile at low and high compositions.[8] According to the theories of Bai *et al.*[9] and Cogswell *et al.*,[10] currents that amount to only a fraction of the exchange current may already be enough to induce a quasi-solid solution, suppressing phase separation and leading to curved voltage profiles. The large surface area in nanomaterials exposes the properties of electrode surfaces, which can depend strongly on the crystal surface plane orientation. A good example is the (0 0 1) surface of anatase TiO_2, which is thermodynamically unfavorable and more likely to be eliminated at the time of crystal growth.[11] By tuning the growth and attaining a large fraction of the reactive (0 0 1) facets the charge rate could be improved in both microcrystalline[12] and nanostructured sheet-like[13−19] forms.

$LiTi_2O_4$ in the pure spinel structure is of interest as an electrode material for Li-ion batteries due its ability to incorporate additional lithium at a voltage of 1.34 V,[20] which is relatively low for titanium oxides, attaining the composition of $Li_2Ti_2O_4$ with a relatively small change in unit cell volume of ~1.1%. From neutron diffraction it is known that in $LiTi_2O_4$ Li occupies the tetrahedral *8a* sites, while lithiation leads to the occupation of the octahedral *16c* sites as well as the migration

* Address correspondence to m.wagemaker@tudelft.nl.

Received for review May 23, 2012 and accepted September 6, 2012.

Published online September 06, 2012
10.1021/nn302278m

of Li ions from the *8a* to *16c* sites to attain the end $Li_2Ti_2O_4$ composition.[21] This migration of Li from the *8a* to *16c* is most likely due to the Coulomb repulsion between Li atoms occupying adjacent *8a* and *16c* sites, which are separated by 1.82 Å.[22] Another member of the spinel family, $Li_4Ti_5O_{12}$, is of even greater interest as an anode material, being already applied at large scale. It is the end member of the solid-solution region of composition $Li_{3+y}Ti_{6-y}O_{12}$ ($0 \leq y \leq 1$), which possesses a defective spinel structure. What makes it attractive as a Li-ion insertion electrode is the "zero strain" property, resulting in excellent cycle life: upon lithiation from the initial state $Li_4Ti_5O_{12}$ to its fully lithiated state $Li_7Ti_5O_{12}$, there is almost no change in lattice parameters (0.2%).[20,23−27] Like in the pure spinel $LiTi_2O_4$, in defective spinel $Li_4Ti_5O_{12}$ all the energetically favorable tetrahedral *8a* sites are occupied by Li (see Figure 1). Additionally one-sixth of the *16d* sites are also occupied by Li at random, while the remaining five-sixths of the *16d* sites are occupied by Ti atoms, which can be represented as $[Li_3]^{8a}[Li_1Ti_5]^{16d}[O_{12}]^{32e}$. Lithiation leads to occupation of all the octahedral *16c* sites and emptying of the tetrahedral *8a* sites to arrive at the end $Li_7Ti_5O_{12}$ composition, which can be represented as $[Li_6]^{16c}[Li_1Ti_5]^{16d}[O_{12}]^{32e}$ (see Figure 1).

Diffraction and NMR studies have demonstrated that above 100 K micrometer-size $Li_{4+x}Ti_5O_{12}$ in equilibrium does not exist as a true two-phase separated system but as a solid solution for diffraction with both $Li_4Ti_5O_{12}$ and $Li_7Ti_5O_{12}$ intimately mixed at nanometer length scales.[28,29] This is attributed to the zero-strain property indicative of very low interfacial energy and strain between the tetrahedral occupied and octahedral occupied coexisting phases. Interface and surface effects appear to play a key role in the nanosized effects, such as the curved voltage profile and reduced miscibility gap in other insertion materials. Interestingly, despite the negligible interface and strain energy, nanosized spinel $Li_{4+x}Ti_5O_{12}$ also leads to the typical "nano"-curved voltage profiles.[30] This raises the question as to what causes the "nano"-curved voltage in $Li_{4+x}Ti_5O_{12}$ and in insertion materials in general. Of additional interest is the observation of stable lithium compositions exceeding $Li_7Ti_5O_{12}$[30−32] albeit for only the first cycles. The possibility of larger capacities is corroborated by bulk *ab initio* calculations performed by Zhong and co-workers[33] showing that it is possible to obtain an *8a* Li occupation in an all-*16c* framework up to a theoretical composition of $Li_{8.5}Ti_5O_{12}$; additional lithium incorporation however was predicted to lead to a negative insertion potential and therefore is impossible to achieve. Recent neutron diffraction measurements have proved that the simultaneous occupation of both *8a* and *16c* (leading to a composition exceeding $Li_7Ti_5O_{12}$) is indeed possible by decreasing the particle size on the order of nanometers, consistent with the increased capacity with decreasing particle size,[30]

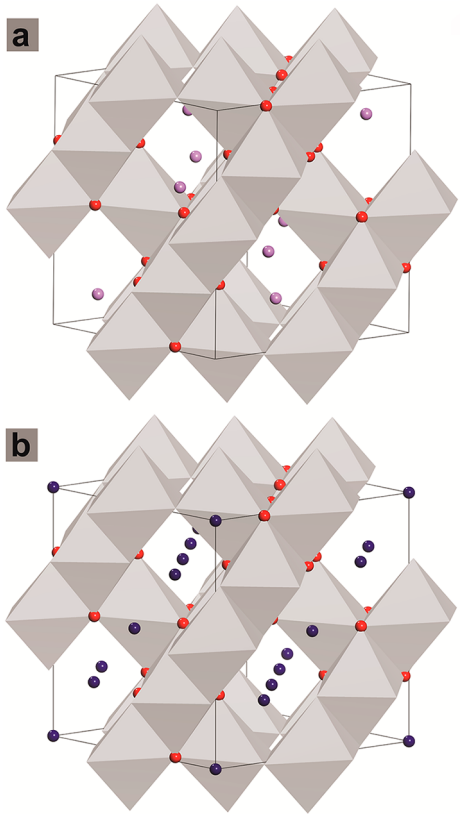

Figure 1. (a) $Li_4Ti_5O_{12}$ and (b) $Li_7Ti_5O_{12}$ structures where the polyhedra indicate $[Li_{1/6}Ti_{5/6}]O_6$ units. Purple in (a) and blue in (b) indicate the tetrahedral *8a* sites and octahedral *16c* sites, respectively.

indicating this to be a surface-related phenomenon. This was more directly proven by epitaxial-grown thin film electrodes showing anisotropic storage capacities and voltages.[32]

In order to investigate the role of the surface on the storage properties of nanosized spinel $Li_{4+x}Ti_5O_{12}$, we calculated the anisotropic surface-dependent voltage profiles and the size-dependent voltage profiles. This gives both fundamental insight into Li-ion storage in nanosized spinel $Li_{4+x}Ti_5O_{12}$ and future prospects for insertion electrodes used in Li-ion batteries. Using density functional theory (DFT) calculations, we studied the impact of different surface orientations on Li-ion storage, which will play a relatively large role in smaller particle sizes. For this study we focused primarily on the defective spinel $Li_4Ti_5O_{12}$ and $Li_7Ti_5O_{12}$ structures, looking at the variation in insertion voltages on Li insertion at the three low-index (1 0 0), (1 1 0), and (1 1 1) surfaces.

RESULTS

Strain and Interface Energy. The role of strain energy in the defective $Li_{4+x}Ti_5O_{12}$ spinel system has been estimated by considering the anisotropic stiffness and lattice mismatch assuming a coherent interface between the coexisting end members $Li_4Ti_5O_{12}$ and

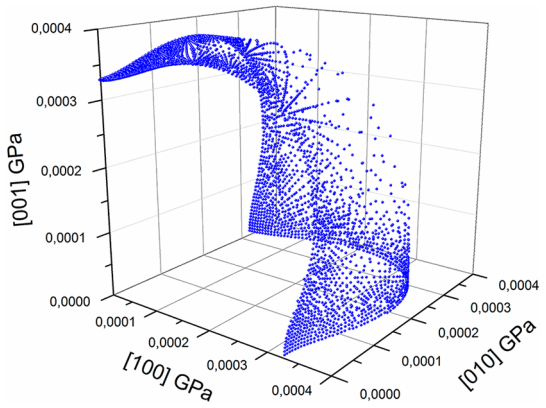

Figure 2. Dependence of the elastic energy on the normal vector of the interface between the two end members $Li_4Ti_5O_7$ and $Li_7Ti_5O_7$ assuming a coherent interface.

$Li_7Ti_5O_{12}$. Assuming the elastic moduli, calculated by DFT GGA (generalized gradient approximation), are the same in both phases, the elastic energy due to the coherent phase coexistence between the end members can be approximated,[34] as recently shown for $LiFePO_4$ by Cogswell *et al.*[10] For cubic materials the elastic energy can be calculated by applying biaxial strain corresponding to the difference in lattice parameters between the end members, which has been worked out analytically for any biaxial strain surface (interface) orientation.[35] Figure 2 displays the resulting dependence of the elastic energy on the interface orientation using the experimentally observed difference in lattice parameters changing from 8.3595 in $Li_4Ti_5O_{12}$ to 8.3538 Å in $Li_7Ti_5O_{12}$.[20,23−27]

Comparing these results to those obtained for $FePO_4/LiFePO_4$,[10] we observe that the elastic energy is almost three orders of magnitude smaller, indicating very little elastic strain energy associated with coherent interfaces in spinel $Li_{4+x}Ti_5O_{12}$. This is mainly the consequence of the very small difference in lattice parameters between the two coexisting phases (0.07%). The elastic strain energy never exceeds 2 meV per unit cell, demonstrating that at room temperature it does not play a significant role. Another energy associated with the existence of a coherent interface between the two coexisting phases is the interface energy as the result of local atomic relaxation near the interface. The resulting values, calculated using DFT, are for all orientations less than 0.02 eV/ Å^2, which is an order of magnitude smaller than the surface energies and the interface energy calculated for $LiFePO_4$.[6] On the basis of this we assume that both the interface energy and elastic strain energy do not play a significant role in the insertion and phase transition mechanism of spinel $Li_{4+x}Ti_5O_{12}$. This is consistent with previous experimental findings that have demonstrated $Li_{4+x}Ti_5O_{12}$ to be nearly a solid solution at room temperature existing as nanoscale domains of the coexisting end phases.[28,29]

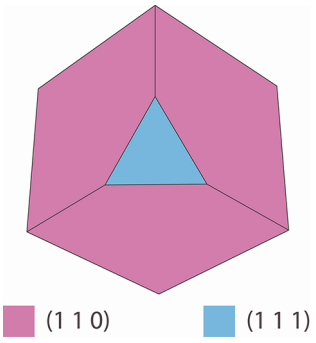

Figure 3. Wulff shape determined from the calculated surface energies of pure $LiTi_2O_4$ spinel.

Surface Energies and Equilibrium Shape. Relaxation of bulk spinel $LiTi_2O_4$ yielded lattice parameters a = 8.374 Å, b = 8.373 Å, and c = 8.374 Å, which differs by ~0.4% from the experimental values.[21] The lowest surface energies were determined to be 1.20 J/m^2 for the (1 0 0) surface a planar arrangement of $Li-O_2-Ti_2-O_2-...-O_2-Li$, 0.58 J/m^2 for the (1 1 0) surface with a planar arrangement of $O_2-Li_2Ti_2O_4-O_2-Ti_2-...-Li_2Ti_2O_4-O_2$, and 0.63 J/m^2 for the (1 1 1) surface with a planar arrangement of $O_3-O-Ti_3-O-O_3-Li-Ti-....-O-O_3$. The lowest energy surfaces were those with minimal loss of coordination to the subsurface TiO_6 octahedra. For symmetric (1 1 0) slabs with surface terminations of $Ti_2-O_2-...-Ti_2$ and $Li_2Ti_2O_4-O_2-...-Li_2Ti_2O_4$ it was possible to make the slab stochiometric by the introduction of Ti and Li surface vacancies, respectively. The surface energy of the surfaces with a Ti vacancy was 1.55 J/m^2, and that with the Li vacancy was 1.98 J/m^2, which is about half the value for similar nonstoichiometric surface terminations, which was determined to be 2.85 and 3.64 J/m^2, respectively, though still much higher than the surface energies for oxygen-terminated surfaces.

The equilibrium shape of spinel $LiTi_2O_4$ was determined using the Wulff construction.[36] The Wulff shape determined on the basis of the surface energies calculated is depicted in Figure 3. The lowest energy (1 1 0) facet made up the major part of the surface of the equilibrium shape, while the higher energy (1 1 1) surface appeared as a smaller facet. The (1 0 0) surface did not appear in the Wulff shape due to its high surface energy. In order to restrict computational time, the higher index planes leading to smaller facets were not considered.

One of the difficulties of modeling the defective spinel $Li_4Ti_5O_{12}$ is the disorder of Li on the *16d* sublattice. For the bulk structure, we selected the lowest energy configuration of Li on the *16d* sublattice, which was determined by calculating all possible configurations in a $Li_{32}Ti_{40}O_{96}$ supercell. Due to the large size of the initial bulk structure and difficulties in determining accurate *16d* positions in the slab with different surface terminations, the equilibrium shape of the defective

spinel $Li_4Ti_5O_{12}$ was not calculated. For the size-dependent voltage curve, which requires the relative contribution of each surface, the equilibrium shape of spinel $LiTi_2O_4$ was assumed.

Strategy to Calculate a Voltage Curve. For the insertion process we assume that lithium addition occurs homogeneously over the surface, starting at the surface. Although this enormously reduces the number of possible configurations, several different schemes for the addition of lithium in $Li_4Ti_5O_{12}(LiTi_2O_4)$ may occur. Of particular interest is the interface between the two coexisting phases, Li on tetrahedral *8a* sites and Li on octahedral *16c* sites. For the calculation of the voltage as a function of composition we consider two schemes. (1) In the first scheme Li is added at the *16c* positions starting from the oxygen-terminated surface and continuing toward the bulk while removing the Li atoms from all *8a* positions next to occupied *16c* sites, including those at the interface between the domains of *16c* and *8a* occupancy, as in Figure 4a. Consequently, in this scheme there are no nearest *8a*−*16c* neighbors. (2) In the second scheme again Li is added at the *16c* positions starting from the surface and continuing toward the bulk while removing the Li atoms from the *8a* positions next to occupied *16c* sites except from the *8a* positions at the interface between domains of *16c* and *8a* occupancy, as in shown Figure 4b. Consequently, in this scheme there are nearest *8a*−*16c* neighbors. For both schemes addition of lithium leads to increasing *16c* occupancy starting at the surface and proceeding into the bulk, the only difference being the presence of *8a*−*16c* nearest neighbors at the interface in the second scheme. On the basis of the Li^+−Li^+ repulsion the second scheme is expected to result in higher energies, hence lower potentials. The lithium composition of the slab was increased stepwise from $Li_4Ti_5O_{12}$-$(LiTi_2O_4)$ toward $Li_7Ti_5O_{12}(Li_2Ti_2O_4)$. Further lithiation was achieved by *8a* occupation in addition to the occupied *16c* sites in the $Li_7Ti_5O_{12}(Li_2Ti_2O_4)$ slab, also assuming that the additional occupancy starts at the surface and continues toward the bulk as shown in panel (c) of Figure 4. After each lithium addition, the average insertion voltage was calculated.

Voltage Curve of Defective Spinel $Li_{4+x}Ti_5O_{12}$. To determine the calculated average plateau voltage, stochiometric slabs of $Li_4Ti_5O_{12}$ and $Li_7Ti_5O_{12}$ with Li occupying all the *8a* and *16c* sites, respectively, were relaxed for the (1 0 0), (1 1 0), and (1 1 1) surfaces. Longer slabs of lengths 25.2, 35.7, and 29.1 Å at the (1 0 0), (1 1 0), and (1 1 1) surface terminations were required in order to maintain the correct stochiometry in which Li at *16d* sites were positioned at regular intervals. A vacuum layer of 15 Å was found to be adequate to remove any spurious interaction between the periodically repeated slabs. The calculated average insertion voltage between slabs having initial and end compositions of $Li_4Ti_5O_{12}$ and $Li_7Ti_5O_{12}$ was determined to be 1.81, 1.58, and 1.77 V for the (1 0 0), (1 1 0), and (1 1 1) surfaces, respectively. The average insertion voltages of the (1 0 0) and (1 1 1) surfaces are significantly larger than the calculated bulk voltage of 1.57 V, which compares well with the experimental value of 1.55 V.[24,27] Using the two strategies schematically displayed in Figure 4a and b and described in the previous section, voltage profiles were calculated by adding lithium stepwise to the slabs with $Li_4Ti_5O_{12}$ and $Li_7Ti_5O_{12}$ compositions terminating at the each of the three surfaces, the results of which are shown in Figure 5.

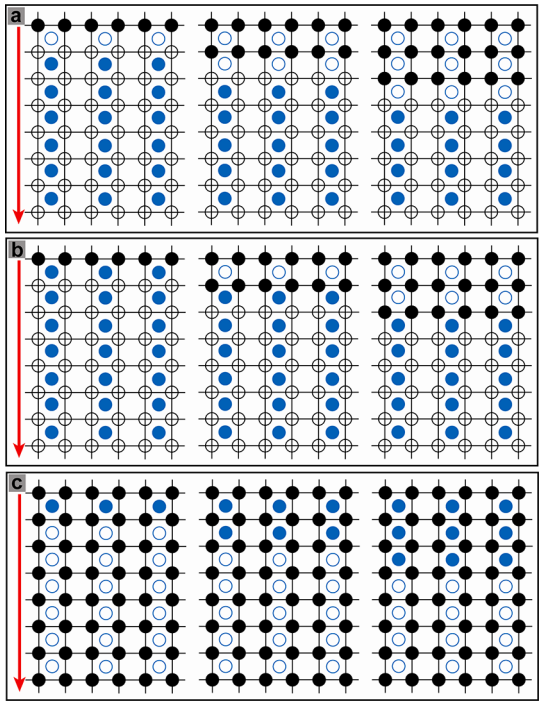

Figure 4. Scheme used to calculate the voltage profiles for Li insertion. The solid blue and black circles represent Li at *8a* and *16c* sites, while the hollow circles indicate vacant *8a* and *16c* sites, respectively. The direction of the bulk is indicated by red arrows. The first strategy depicted in panel (a) represents the sequential addition of Li to layers containing vacant *16c* sites at increasing depths from the surface without introducing nearest *8a*−*16c* neighbors at the interface between domains having *8a* and *16c* occupancy. Panel (b) represents the second strategy for sequential Li insertion where nearest *8a*−*16c* neighbors are present at the interface between domains having *8a* and *16c* occupancy. Panel (c) shows the sequential addition of Li to layers with vacant *8a* sites.

The (1 0 0) surface was found to be the most energetically favorable for initial Li insertion into $Li_4Ti_5O_{12}$, as seen in Figure 5a. This is reflected in the high voltage, >3 V, on Li insertion into the first two subsurface layers, making it more favorable compared to insertion into the bulk. Li insertion into the subsurface layers of the (1 1 0) and (1 1 1) $Li_4Ti_5O_{12}$ surfaces shown in Figure 5b and c also allows Li addition at voltages between 2.5 and 3 V, larger than the average insertion voltage and consistent with what is observed experimentally.[30] The voltage curves calculated for the (1 0 0) surface shown in Figure 5a reveal negligible

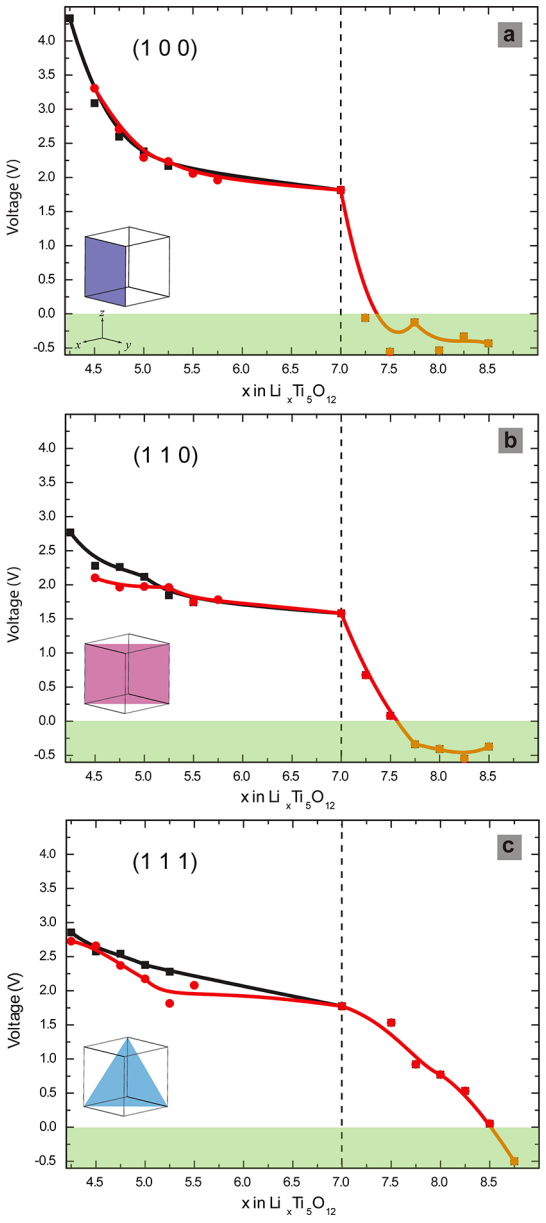

Figure 5. Calculated voltage profiles for the $Li_4Ti_5O_{12}$–$Li_7Ti_5O_{12}$ system. Voltage curves in (a), (b), and (c) correspond to particles whose facets all have (1 0 0), (1 1 0), and (1 1 1) surfaces, respectively, wherein the black and red curves correspond to the absence and presence of nearest *8a*–*16c* neighbors at the interface during Li-ion insertion. The curves have been used as a guide to the eye and are not an average value. The green-shaded area in each graph represents the region under 0 V where no Li intercalation is feasible.

differences between the two insertion schemes, despite the presence of nearest *8a*–*16c* neighbors in the second scheme (Figure 4b, represented by the red curve in Figure 5a). This is due to the relaxation of the Li atoms initially at adjoining *8a* sites, toward vacant *16c* sites in the layers below (*8a*–*16c*, Figures 6e–h). The shortest Li^+–Li^+ distances for Figures 6a–d (black curve, Figure 5a) are 2.979, 2.756, 2.799, and 2.689 Å, respectively, while for Figures 6e–h (red curve, Figure 5a) they are 2.481, 2.513, 2.345, and 2.471 Å, respectively. Apparently, the Li-ion separation at the near surface environment for the (1 0 0) surface for both insertion schemes is large enough to avoid a significant energy penalty due to Coulombic repulsion. For the (1 1 0) surface termination however, the second scheme leads to lower voltages compared to the first scheme, comparing the red and black curves in Figure 5b, respectively. In this case the presence of adjoining *8a*–*16c* Li-ions at the interface between domains of *16c* and *8a* occupancy (second scheme) results in higher energy penalties and hence lower voltages as compared to leaving empty sites at the interface separating the *16c* and *8a* occupancy domains (first scheme). This can be attributed to the smaller lattice spacing of layers in the (1 1 0)-terminated $Li_4Ti_5O_{12}$ slabs (Supporting Information Figure S1). Despite the relaxation of the Li atoms from the adjoining *8a* sites, toward vacant *16c* sites in the layers below, the small lattice spacing still results in relatively small *8a*–*16c* distances (Supporting Information Figure S1e–h).

The $Li_7Ti_5O_{12}$ composition can be exceeded by adding Li to vacant *8a* sites in the (1 0 0), (1 1 0), and (1 1 1) slabs having all *16c* sites occupied (composition $Li_7Ti_5O_{12}$). The calculated voltage profiles in Figure 5a–c indicate that, before reaching negative voltages, this is possible up to compositions of $Li_{7.3}Ti_5O_{12}$, $Li_{7.5}Ti_5O_{12}$, and $Li_{8.5}Ti_5O_{12}$ for the (1 0 0), (1 1 0), and (1 1 1) surfaces, respectively. Therefore, the calculations predict that the surface is able to host capacities that exceed the $Li_7Ti_5O_{12}$ bulk composition. This is consistent with the experimental finding that the capacity scales with the surface area and that additional *8a* occupation in an all-*16c* occupied lattice is possible.[30] The larger capacity appears mainly the result of the (1 1 1) surface, consistent with the larger capacity found with electrochemically charged epitaxial-grown films.[32] In Figures 7a–d the nearest Li^+–Li^+ (*8a*–*16c*) distance in the (1 1 1)-terminated slab is 2.196 Å at the surface and gradually approaches the bulk value (1.82 Å) away from the surface.

Size-dependent voltage profiles shown in Figure 8 were calculated by taking into account the relative contributions of the Wulff shape surface sites with respect to bulk sites (voltages) when the particle size exceeds the extent of the slab thickness. Here it is assumed that bulk sites result in a constant voltage, which is true for intraparticle moving phase boundaries. Although this phase transformation mechanism is questionable for nanomaterials,[8,10,37] since the voltage changes only in the range of 10 meV,[8,30] the assumption of a constant bulk voltage in Figure 8 appears reasonable. By increasing the particle size the number of bulk sites increases, and hence the capacity of the constant voltage plateau increases, thereby reducing the relative amount of surface storage that is responsible for the voltages above and below the voltage plateau. In Figure 8 the voltage curves are plotted for particle sizes up to 100 nm, based on the relative contributions of the

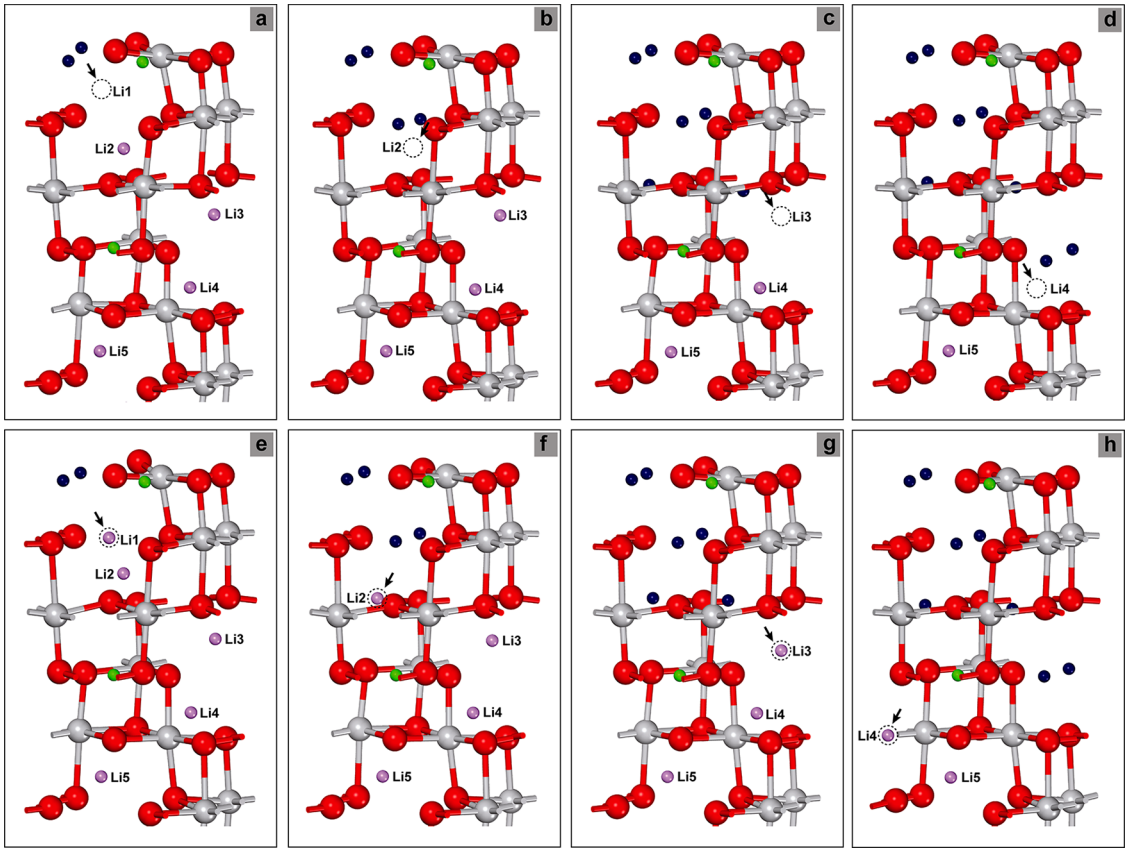

Figure 6. Relaxed surface structures corresponding to the sequential addition of Li to the (1 0 0) surface of $Li_4Ti_5O_{12}$ at vacant *16c* sites. Panels (a) to (d) depict Li addition to the first four layers at increasing depths from the surface with the absence of nearest *8a*−*16c* neighbors at the interface. Panels (e) to (h) correspond to Li addition to the first four layers at increasing depths from the surface with the presence of nearest *8a*−*16c* neighbors at the interface. The large red and gray spheres are O and Ti atoms, respectively. The smaller blue, violet, and green spheres correspond to Li atoms at *16c*, *8a*, and *16d* sites, respectively. The dotted circles refer to *8a* Li atoms, whose presence determines the *8a*−*16c* interface.

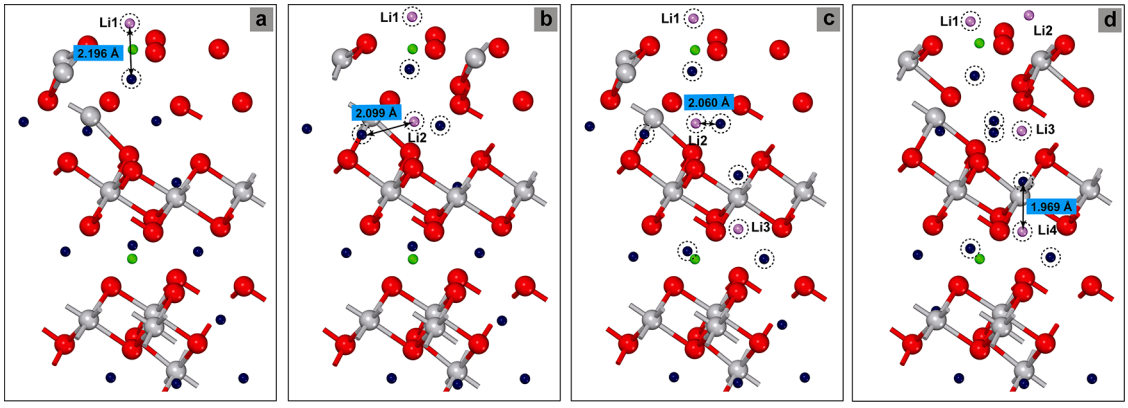

Figure 7. Relaxed surface structures corresponding to the sequential addition of Li to the (1 1 1) surface of $Li_7Ti_5O_{12}$ at vacant *8a* sites. Panels (a) to (d) depict Li addition to *8a* sites in the first four layers at increasing depths from the surface in the presence of all occupied *16c* sites. The large red and gray spheres are O and Ti atoms, respectively. The smaller blue, violet, and green spheres correspond to Li atoms at *16c*, *8a*, and *16d* sites, respectively. The dotted circles refer to Li atoms whose presence determines the *8a*−*16c* nearest neighbors.

(1 1 0) and (1 1 1) surfaces in the Wulff shape (Figure 3) and assuming the lowest energy insertion scheme (scheme 1 shown in Figure 4a). The voltages above the bulk voltage plateau at low compositions are mainly due to Li insertion of *16c* sites at the (1 1 0) surface, and the voltages below the bulk voltage plateau are due to Li insertion into vacant *8a* sites at the (1 1 1) surface, resulting in compositions exceeding $Li_7Ti_5O_{12}$. Voltage curves were also calculated for Li insertion into the (1 0 0), (1 1 0), and (1 1 1) surfaces of pure spinel $LiTi_2O_4$ and $Li_2Ti_2O_4$, which are included in the Supporting Information (Supporting Information text and Figure S2).

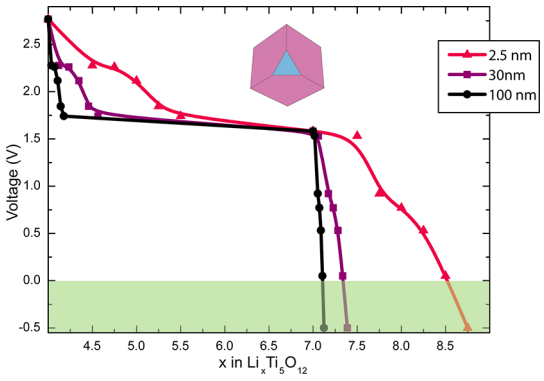

Figure 8. The pink voltage curve corresponds to a composite for particles combining Li insertion into vacant *16c* sites in a $Li_4Ti_5O_{12}$ host without nearest *8a*−*16c* neighbors at the interface from (1 1 0) facets and Li insertion into a $Li_7Ti_5O_{12}$ host with vacant *8a* sites from (1 1 1) facets corresponding to the Wulff shape. The purple and black curves correspond to particle sizes of 30 and 100 nm. The green-shaded area represents the region under 0 V, where no Li intercalation is feasible.

DISCUSSION

Curved Voltage Profile. The origin of the sloping voltage profile and corresponding changes in solubility limits encountered for very small nanostructured Li-insertion materials has recently garnered significant scientific interest. The reduced miscibility gap has been attributed to the presence of the interface between coexisting phases[3−6] that is present through the first-order phase transition. This is also suggested to be the origin of the curved voltage profile because of the shorter compositional domain where the voltage is constant, reflecting the reduced miscibility gap. An additional explanation for the curved voltage profile is the contribution of the surface energy to the voltage of nanosized particles. Surface free energies become increasingly important in affecting voltage profiles as electrode particles approach nanometer dimensions. The plateau voltage of a first-order phase transformation depends on crystallite dimensions,[7,38] and a distribution of crystallite sizes consequently leads to a spectrum of transformation voltages that produces a sloping voltage profile similar to that of a solid solution.[7] In addition, the experimentally observed curved voltage profile may be the result of entropy effects. These arise due to particle by particle charging/discharging mechanisms that are predicted for nanoparticles,[8] and also because of rate effects that are predicted to already play a role at current densities that are only a few percent of the exchange current density.[9,10] In the calculations shown in Figures 5 and 8 none of these phenomena are incorporated. Therefore, the curved voltage profiles resulting from the present surface calculations indicate that another mechanism is at least contributing significantly to the curved voltage profile of nanospinel lithium titanium oxides. Depending on the orientation of the surface, the voltage gradually changes toward the bulk voltage over a distance on the order of a few nanometers, as illustrated by Figure 5. This is the consequence of the difference of the near surface environment from the bulk environment which extends approximately a nanometer into the particle. Depending on the specific surface orientation, the atomic arrangement at the lithiated surface is able to relax in such a way that it increases the nearest Li^+-Li^+ distances, thereby lowering the energy, leading to higher insertion voltages. Naturally, this ability gradually decreases toward the bulk, explaining the continuous decrease of the voltage from the high initial voltages toward the bulk voltage as observed in Figures 5 and 8. The resulting particle size dependent voltage profiles in Figure 8 are in qualitative agreement with those observed experimentally, exhibiting the increasing curved voltage profile with decreasing particle size.[30] Our prediction that the surface storage properties depend on the specific surface orientation leading to different voltage profiles is corroborated experimentally by a recent study performed by Hirayama and co-workers[32] in which epitaxial-grown spinel $Li_4Ti_5O_{12}$ thin films were prepared. The electrochemistry revealed sloping voltage curves, depending on the surface orientation, with a reduced plateau reminiscent of those observed for nanocrystalline spinel $Li_4Ti_5O_{12}$.[30] In particular the voltage curve measured for the (1 1 0) surface bears a marked resemblance to the one calculated for the (1 1 0) -terminated slab in this study, Figure 5b, showing a sloped voltage region at lower capacities and a constant voltage region at higher capacities. Also the higher capacity of the (1 1 1) surface observed experimentally is reproduced by the calculations shown in Figure 5c.

The finding that surface-dependent insertion storage properties deviate from the bulk properties is expected to be a general phenomenon for insertion electrode materials. A computational study on olivine $LiFePO_4$ also indicates that the redox potentials depend on the orientation of the surface plane.[39] Therefore, we suggest that the commonly observed curved voltage shape in nanostructured insertion materials that exhibit a first-order phase transition is at least partly the consequence of the gradual transition from the surface to bulk environment. This explains why the capacity of the curved voltage profile (deviating from the voltage plateau) scales with the particle surface area[30] and why the voltages deviate from the bulk value. On the basis of our findings we suggest the following insertion mechanism in spinel lithium titanium oxides: Upon lithium insertion first the low chemical potential (high voltage) surfaces are inserted, followed by the bulk, which leads to the voltage plateau, and finally the high chemical potential (low voltage) surfaces are inserted. The requirement for the insertion mechanism is facile diffusion of the Li-ions through the solid-state matrix of the spinel structure. In particular this appears to be the case for compositions between $x = 0$ and $x = 3$ in $Li_{4+x}Ti_5O_{12}$, where the

migration barrier was experimentally determined to have values close to 0.3 eV.[29] Additional lithium storage at the near surface region of specific surfaces explains the higher capacities on reducing the particle size. These surfaces are responsible for capacities exceeding the maximum bulk composition of $Li_7Ti_5O_{12}$, up to a composition of $Li_{8.5}Ti_5O_{12}$. This leads to capacities close to the theoretical composition based on the Ti^{3+}/Ti^{4+} redox couple. The explanation is that the surface relaxation at these specific surfaces allows lithium storage at a lower energy and, hence, at a higher voltage compared to the same compositions in the bulk. By particle size reduction, the surfaces represent a relatively larger part of the total capacity, explaining the larger capacities of smaller particles. Note that the shape determines the observed properties because of the anisotropic surface storage. Hence, the calculations predict that shape and nanosizing can be used to tailor the storage properties of capacity and voltage.

Surface Reconstruction. For $Li_{4+x}Ti_5O_{12}$ ($x \geq 3$) reducing the particle size below 20 nm leads to a decrease in the reversible capacity.[30,40] Neutron diffraction data revealed for 12 nm particles a partial *8a* occupation in addition to full *16c* occupation, leading to an average composition as high as $Li_{8.1}Ti_5O_{12}$.[30] Assuming that the additional *8a* occupancy predominantly occurs near the surface, consistent with our calculations, this would lead to local surface compositions exceeding the average $Li_{8.1}Ti_5O_{12}$ composition. Because both bulk *ab initio* calculations[33] and the present surface calculations predict negative insertion voltages at compositions larger than $Li_{8.5}Ti_5O_{12}$, this should be considered the upper limit for the local composition near the surface. Loss of reversible capacity for nanoparticles appeared irrespective of the window of battery cycling;[30] that is, for potential windows of 2.5−0.9 and 2.5−0.05 V the loss of capacity was the same, indicating that the formation of a solid electrolyte interface was not responsible for the capacity loss. Because the capacity loss appears to scale with the particle surface area, it was suggested that the irreversible capacity loss was due to structural reconstruction at the surface.[30,41] This was confirmed by recent cyclic voltammetry performed on epitaxial (1 1 0) and (1 1 1) oriented films of $Li_4Ti_5O_{12}$.[32] During the first cathodic scan additional reduction peaks were observed, which disappeared on further cycling and were ascribed to a reconstruction of the surface on the first discharge. The peak position differed depending on the surface orientation, indicating that the surface reconstruction is anisotropic.[32] In our study we have determined that the maximum amount of Li that can be incorporated is $Li_{7.3}Ti_5O_{12}$ for the (1 0 0), $Li_{7.5}Ti_5O_{12}$ for the (1 1 0), and $Li_{8.5}Ti_5O_{12}$ for the (1 1 1) facet assuming an insertion voltage limit just above 0 V. Therefore, it is possible that the additional incorporation of Li in specific surface facets and their subsequent reconstruction may lead to (partially) irreversibly trapped lithium, explaining the irreversible capacity loss. An energetically feasible reaction may be the formation of rocksalt $LiTiO_2$[42] and lithium oxide:

$$Li_9Ti_5O_{12} \rightarrow 5LiTiO_2\ (\text{rocksalt}) + 2Li_2O$$

We determined the enthalpy of formation of rock salt $LiTiO_2$ and Li_2O to be −0.26 eV per Li atom. Possibly, initial lithium insertion causes this phase transformation at the surface. It is unclear if the rock salt formation is partially reversible. The reversible formation of Li_2O is well-known for several nanosized transition metal oxides.[43] However, that involves the decomposition of metal oxides and the formation of Li_2O during Li insertion and the re-formation of the metal oxides on extraction. Although such conversion reactions do not appear to exist for titanium oxides at present, it would be interesting to investigate the possibility of improvement of the reversible capacity of $Li_4Ti_5O_{12}$. This would entail the search for surfaces that are less prone to surface reconstruction using first-principles calculations and subsequent surface-specific synthesis of such materials. Eliminating blocked facets and using surfaces more favorable to reversible lithium insertion would offer interesting possibilities, creating cheap, high-capacity, and high-power anode materials for Li-ion batteries; however, more research is required to make this a reality.

CONCLUSIONS

We have investigated Li-ion insertion into the surfaces of spinel lithium titanium oxides. The calculated voltage profile of the defective spinel $Li_4Ti_5O_{12}$ reveals that it is energetically more favorable to insert lithium into the (1 0 0) surfaces, leading to initially high voltages due to surface storage. The maximum observed bulk composition $Li_7Ti_5O_{12}$ can be surpassed by Li storage at the (1 1 1) surface facilitated by surface relaxation effects. This explains the higher capacities of nanosized spinel titanium oxides at voltages below the bulk voltage plateau. On the basis of this we predict that increasing the relative amount of (1 1 1) facets by reducing the size and tailoring the shape will significantly increase the storage capacity. Whether this capacity can be achieved reversibly depends on irreversible surface reactions at these high compositions. The calculations show that the surface properties, differing from the bulk properties, extend up to a few nanometers into the particles. This rationalizes that many of the nanosize properties are in fact the consequence of the relatively large contribution of the surfaces in nanomaterials. The calculated anisotropic and size-dependent voltage profiles are in good agreement with recent experiments. The calculations further predict that the voltage may be tailored if the relative amount of specific surface orientations can be controlled by the shape of the nanoparticles. By increasing

the low-voltage and high-capacity surfaces in nanostructured spinel $Li_4Ti_5O_{12}$ used as a negative electrode, the voltage window *versus* a positive electrode material can potentially be increased, leading to a higher energy and power density of the battery. Thereby, the calculations give insight into the possibilities to tailor voltage and capacity of lithium insertion electrodes by means of the nanosize and shape.

In addition higher lithium concentrations in specific surface facets may result in their subsequent reconstruction into the rock salt $LiTiO_2$ phase, leading to irreversibly trapped lithium, which would explain the irreversible capacity loss observed. The calculations reveal that the curved voltage shape of nanosized spinel $Li_{4+x}Ti_5O_{12}$ is at least largely the result of a distribution in lithium environments near the surface depending on the proximity and the orientation of the surface. The generality of this phenomenon suggests that the surface may be at least partly responsible for the curved voltage shape in nanostructured insertion materials.

METHODS

Computational Details. All ground-state energies were calculated using the generalized gradient approximation to the density functional theory[44] as implemented in the Vienna *ab initio* simulation package (VASP).[45] The projector augmented method (PAW)[46] is used to describe the electronic-ion−core interactions. The cutoff energy was set at 400 eV for accurate calculations. Since the material is nonmagnetic, spin polarizations were not included in the calculations. The convergence of total energy with respect to the *k*-point sampling was taking into consideration, thereby ensuring the total energy was converged to within 10^{-4} eV per formula unit. Because VASP calculations are performed, periodic slabs were constructed in which a set of infinite layers separated by vacuum layers is repeated periodically along the surface normal. Slabs of pure spinel $LiTi_2O_4$ with Li occupying all the *8a* tetrahedral sites were modeled for low-index (1 0 0), (1 1 0), and (1 1 1) surface terminations. According to the definition of Tasker,[47] only type 2 symmetrically arranged surfaces were considered, so that there was no dipole moment perpendicular to the surface. As a consequence of the symmetric arrangement of the planes in the slab, their composition was nonstochiometric, *i.e.*, was not an integral multiple of the $LiTi_2O_4$ formula unit. The (1 0 0), (1 1 0), and (1 1 1) slabs were 16−18, 11−14, and 15−20 Å long for various surface terminations. Four central layers of each slab were frozen while the rest of the atoms at the surface layers at both ends of the slab were allowed to relax. A vacuum layer of 13 Å for the (1 0 0) and (1 1 1) surfaces and 10 Å for the (1 1 0) surface was found to be adequate to remove any spurious interaction between the periodically repeated slabs. The surface energies were calculated by dividing the difference of the energy of the slab and an equal number of formula units of $LiTi_2O_4$ with the surface area of the slab taking both sides of the slab into consideration.

Wulff Shape. Determination of the Wulff shape entails the construction of a polar plot of the surface energies by drawing along each crystallographic direction a vector whose length is proportional to the surface energy in that direction. At the end of each vector a plane perpendicular to the vector direction is drawn. The shape enclosed by the planes gives the equilibrium shape of the crystal, as shown for $LiTi_2O_4$ spinel in Figure 3.

Insertion Voltage. The average insertion voltage can be described in terms of the difference in Gibbs free energy (ΔG) for the insertion reaction as[48]

$$\bar{V} = \frac{-\Delta G}{(x_2 - x_1)F}$$

where F is Faraday's constant and x_1 and x_2 are the two limit Li compositions between which insertion occurs, where $x_2 > x_1$. Further simplification can be achieved by the assumption that the changes in volume and entropy are small during this reaction, wherein $\Delta G = \Delta E + P\Delta V - T\Delta S$. $P\Delta V$ is on the order of 10^{-5} eV, and the internal energy ΔE is on the order of a few eV per molecule. $T\Delta S$ is on the order of the thermal energy, which is also much smaller than ΔE. As a result, the average insertion voltage can be approximated as

$$\bar{V} = \frac{-\Delta E}{(x_2 - x_1)F}$$

where ΔE is the calculated total energy difference of the two insertion limits taking metallic Li as a reference. To support the assumption that entropy plays a relatively insignificant role compared to the differences in configurational energy, the entropy of the available sites in all models was approximated by the lattice gas model. This resulted in values less than 14 meV for all surfaces considered, which is two orders of magnitude smaller when compared to the surface storage effects found at present. In addition, the vibrational entropy in bulk and surface sites was determined using DFT. This contribution is also relatively small, never exceeding 8 meV.

Strain Energy. For the cubic symmetry of these spinel structures the number of independent elastic constants reduces to three (c11, c12, and c44 using the Voigt notation). Using DFT GGA these constants were determined by applying uniform hydrostatic pressure, uniaxial strain, and pure shear strain.[49] Assuming the elastic moduli are the same in both phases, the elastic energy due to the coherent phase coexistence between the end members was approximated.[10,34,35]

Interfacial Energy. *Ab initio* DFT GGA calculations were used to calculate the excess energy associated with a coherent interface perpendicular to the [100] direction using cells containing periodic regions of $Li_4Ti_5O_{12}$ separated by regions of $Li_7Ti_5O_{12}$. In two directions the lattice parameters were fixed, and in the third direction the lattice parameter was allowed to relax. By subtracting similarly relaxed bulk energies with the same volume, elastic energy contributions cancel out and interface energy follows by dividing the resulting energy by the interface area.[6] Further details on these calculations can be found in the Supporting Information.

Conflict of Interest: The authors declare no competing financial interest.

Acknowledgment. Financial support from The Netherlands Organization for Scientific Research (NWO) is acknowledged for the CW-VIDI grant of M.W. The assistance of J. Heringa is gratefully acknowledged.

Supporting Information Available: Voltage profiles calculated for the pure spinel $LiTi_2O_4$ and $Li_2Ti_2O_4$ and supporting figures and text have been included and are available free of charge *via* the Internet at http://pubs.acs.org.

REFERENCES AND NOTES

1. Arico, A. S.; Bruce, P.; Scrosati, B.; Tarascon, J. M.; Van Schalkwijk, W. Nanostructured Materials for Advanced Energy Conversion and Storage Devices. *Nat. Mater.* **2005**, *4*, 366–377.
2. Maier, J. Nanoionics: Ion Transport and Electrochemical Storage in Confined Systems. *Nat. Mater.* **2005**, *4*, 805–815.
3. Meethong, N.; Huang, H. Y. S.; Speakman, S. A.; Carter, W. C.; Chiang, Y. M. Strain Accommodation during Phase Transformations in Olivine-Based Cathodes as a Materials Selection Criterion for High-Power Rechargeable Batteries. *Adv. Funct. Mater.* **2007**, *17*, 1115–1123.
4. Wagemaker, M.; Singh, D. P.; Borghols, W. J. H.; Lafont, U.; Haverkate, L.; Peterson, V. K.; Mulder, F. M. Dynamic Solubility Limits in Nanosized Olivine $LiFePO_4$. *J. Am. Chem. Soc.* **2011**, *133*, 10222–10228.

5. Burch, D.; Bazant, M. Z. Size-Dependent Spinodal and Miscibility Gaps for Intercalation in Nanoparticles. *Nano Lett.* **2009**, *9*, 3795–3800.
6. Wagemaker, M.; Mulder, F. M.; van der Ven, A. The Role of Surface and Interface Energy on Phase Stability of Nano-sized Insertion Compounds. *Adv. Mater.* **2009**, *21*, 1–7.
7. Van der Ven, A.; Wagemaker, M. Effect of Surface Energies and Nano-Particle Size Distribution on Open Circuit Voltage of Li-Electrodes. *Electrochem. Commun.* **2009**, *11*, 881–884.
8. Dreyer, W.; Jamnik, J.; Guhlke, C.; Huth, R.; Moskon, J.; Gaberscek, M. The Thermodynamic Origin of Hysteresis in Insertion Batteries. *Nat. Mater.* **2010**, *9*, 448–453.
9. Bai, P.; Cogswell, D. A.; Bazant, M. Z. Suppression of Phase Transformations in $LiFePO_4$ during Battery Discharge. *Nano Lett.* **2011**, *11*, 4890–4896.
10. Cogswell, D. A.; Bazant, M. Z. Coherency Strain and the Kinetics of Phase Separation in $LiFePO_4$ Nanoparticles. *ACS Nano* **2012**, *6*, 2215–2225.
11. Yin, Y.; Alivisatos, A. P. Colloidal Nanocrystal Synthesis and the Organic-Inorganic Interface. *Nature* **2005**, *437*, 664–670.
12. Yang, H. G.; Sun, C. H.; Qiao, S. Z.; Zou, J.; Liu, G.; Smith, S. C.; Cheng, H. M.; Lu, G. Q. Anatase TiO_2 Single Crystals with a Large Percentage of Reactive Facets. *Nature* **2008**, *453*, 638–641.
13. Zhang, D. Q.; Li, G. S.; Yang, X. F.; Yu, J. C. A Micrometer-Size TiO_2 Single-Crystal Photocatalyst with Remarkable 80% Level of Reactive Facets. *Chem. Commun.* **2009**, 4381–4383.
14. Han, X. G.; Kuang, Q.; Jin, M. S.; Xie, Z. X.; Zheng, L. S. Synthesis of Titania Nanosheets with a High Percentage of Exposed (001) Facets and Related Photocatalytic Properties. *J. Am. Chem. Soc.* **2009**, *131*, 3152–3153.
15. Liu, G.; Yang, H. G.; Wang, X. W.; Cheng, L. N.; Pan, J.; Lu, G. Q.; Cheng, H. M. Visible Light Responsive Nitrogen Doped Anatase TiO_2 Sheets with Dominant {001} Facets Derived from Tin. *J. Am. Chem. Soc.* **2009**, *131*, 12868–12869.
16. Yang, H. G.; Liu, G.; Qiao, S. Z.; Sun, C. H.; Jin, Y. G.; Smith, S. C.; Zou, J.; Cheng, H. M.; Lu, G. Q. Solvothermal Synthesis and Photoreactivity of Anatase TiO_2 Nanosheets with Dominant {001} Facets. *J. Am. Chem. Soc.* **2009**, *131*, 4078–4083.
17. Dai, Y. Q.; Cobley, C. M.; Zeng, J.; Sun, Y. M.; Xia, Y. N. Synthesis of Anatase TiO_2 Nanocrystals with Exposed {001} Facets. *Nano Lett.* **2009**, *9*, 2455–2459.
18. Wu, B. H.; Guo, C. Y.; Zheng, N. F.; Xie, Z. X.; Stucky, G. D. Nonaqueous Production of Nanostructured Anatase with High-Energy Facets. *J. Am. Chem. Soc.* **2008**, *130*, 17563–17567.
19. Chen, J. S.; Tan, Y. L.; Li, C. M.; Cheah, Y. L.; Luan, D. Y.; Madhavi, S.; Boey, F. Y. C.; Archer, L. A.; Lou, X. W. Constructing Hierarchical Spheres from Large Ultrathin Anatase TiO_2 Nanosheets with Nearly 100% Exposed (001) Facets for Fast Reversible Lithium Storage. *J. Am. Chem. Soc.* **2010**, *132*, 6124–6130.
20. Colbow, K. M.; Dahn, J. R.; Haering, R. R. Structure and Electrochemistry of the Spinel Oxides $LiTi_2O_4$ and $Li_{4/3}Ti_{5/3}O_4$. *J. Power Sources* **1989**, *26*, 397–402.
21. Cava, R. J.; Murphy, D. W.; Zahurak, S.; Santoro, A.; Roth, R. S. The Crystal-Structures of the Lithium-Inserted Metal-Oxides $Li_{0.5}TiO_2$ Anatase, $LiTi_2O_4$ Spinel, and $Li_2Ti_2O_4$. *J. Solid State Chem.* **1984**, *53*, 64–75.
22. Wagemaker, M.; Van Der Ven, A.; Morgan, D.; Ceder, G.; Mulder, F. M.; Kearley, G. J. Thermodynamics of Spinel Li_xTiO_2 from First Principles. *Chem. Phys.* **2005**, *317*, 130–136.
23. Deschanv, A.; Raveau, B.; Sekkal, Z. Synthesis and Crystallographic Study of New Solid Solution of Spinel $Li_{1+x}Ti_{2-x}O_4 \leq x \leq 0.33_3$. *Mater. Res. Bull.* **1971**, *6*, 699–704.
24. Scharner, S.; Weppner, W.; Schmid-Beurmann, P. Evidence of Two-Phase Formation Upon Lithium Insertion into the $Li_{1.33}Ti_{1.67}O_4$ Spinel. *J. Electrochem. Soc.* **1999**, *146*, 857–861.
25. Ohzuku, T.; Ueda, A.; Yamamoto, N. Zero-Strain Insertion Material of $Li[Li_{1/3}Ti_{5/3}]O_4$ for Rechargeable Lithium Cells. *J. Electrochem. Soc.* **1995**, *142*, 1431–1435.
26. Johnston, D. C. Superconducting and Normal State Properties of $Li_{1+\chi}$ $Ti_{2-\chi}$ O_4 Spinel Compounds. I. Preparation, Crystallography, Superconducting Properties, Electrical-Resistivity, Dielectric Behavior, and Magnetic-Susceptibility. *J. Low Temp. Phys.* **1976**, *25*, 145–175.
27. Ferg, E.; Gummow, R. J.; Dekock, A.; Thackeray, M. M. Spinel Anodes for Lithium-Ion Batteries. *J. Electrochem. Soc.* **1994**, *141*, L147–L150.
28. Wagemaker, M.; Simon, D. R.; Kelder, E. M.; Schoonman, J.; Ringpfeil, C.; Haake, U.; Lützenkirchen-Hecht, D.; Frahm, R.; Mulder, F. M. A Kinetic Two-Phase and Equilibrium Solid Solution in Spinel $Li_{4+x}Ti_5O_{12}$. *Adv. Mater.* **2006**, *18*, 3169–3173.
29. Wagemaker, M.; van Eck, E. R. H.; Kentgens, A. P. M.; Mulder, F. M. Li-Ion Diffusion in the Equilibrium Nanomorphology of Spinel $Li_{4+x}Ti_5O_{12}$. *J. Phys. Chem. B* **2009**, *113*, 224–230.
30. Borghols, W. J. H.; Wagemaker, M.; Lafont, U.; Kelder, E. M.; Mulder, F. M. Size Effects in the $Li_{4+x}Ti_5O_{12}$ Spinel. *J. Am. Chem. Soc.* **2009**, *131*, 17786–17792.
31. Ge, H.; Li, N.; Li, D. Y.; Dai, C. S.; Wang, D. L. Electrochemical Characteristics of Spinel $Li_4Ti_5O_{12}$ Discharged to 0.01 V. *Electrochem. Commun.* **2008**, *10*, 719–722.
32. Hirayama, M.; Kim, K.; Toujigamori, T.; Cho, W.; Kanno, R. Epitaxial Growth and Electrochemical Properties of $Li_4Ti_5O_{12}$ Thin-Film Lithium Battery Anodes. *Dalton Trans.* **2011**, *40*, 2882–2887.
33. Zhong, Z. Y.; Ouyang, C. Y.; Shi, S. Q.; Lei, M. S. *Ab Initio* Studies on $Li_{4+x}Ti_5O_{12}$ Compounds as Anode Materials for Lithium-Ion Batteries. *ChemPhysChem* **2008**, *9*, 2104–2108.
34. Khachaturyan, A. G. *Theory of Structural Transformations in Solids*; Dover Publications: New York, 2008.
35. Hammerschmidt, T.; Kratzer, P.; Scheffler, M. Elastic Response of Cubic Crystals to Biaxial Strain: Analytic Results and Comparison to Density Functional Theory for InAs. *Phys. Rev. B* **2007**, *75*, 235328.
36. Wulff, G. On the Question of Speed of Growth and Dissolution of Crystal Surfaces. *Z. Kristallogr.* **1901**, *34*, 449–530.
37. Wagemaker, M.; Borghols, W. J. H.; Mulder, F. M. Large Impact of Particle Size on Insertion Reactions, a Case of Anatase Li_xTiO_2. *J. Am. Chem. Soc.* **2007**, *129*, 4323–4327.
38. Jamnik, J.; Maier, J. Nanocrystallinity Effects in Lithium Battery Materials - Aspects of Nano-Ionics. Part IV. *Phys. Chem. Chem. Phys.* **2003**, *5*, 5215–5220.
39. Wang, L.; Zhou, F.; Meng, Y. S.; Ceder, G. First-Principles Study of Surface Properties of $LiFePO_4$: Surface Energy, Structure, Wulff Shape, and Surface Redox Potential. *Phys. Rev. B* **2007**, *76*, 165435.
40. Kavan, L.; Prochazka, J.; Spitler, T. M.; Kalbac, M.; Zukalova, M. T.; Drezen, T.; Gratzel, M. Li Insertion into $Li_4Ti_5O_{12}$ (Spinel) - Charge Capability *vs.* Particle Size in Thin-Film Electrodes. *J. Electrochem. Soc.* **2003**, *150*, A1000–A1007.
41. Erdman, N.; Poeppelmeier, K. R.; Asta, M.; Warschkow, O.; Ellis, D. E.; Marks, L. D. The Structure and Chemistry of the TiO_2-Rich Surface of $SrTiO_3$(001). *Nature* **2002**, *419*, 55–58.
42. Lecerf, A. Sur Quelques Proprietes Chimiques Des Oxydes TiO Et Ti_2O_3 - Preparation Et Etudes De Nouveaux Composes Ternaires Oxygenes Du Titane Trivalent. *Ann. Chim.* **1962**, *7*, 513.
43. Poizot, P.; Laruelle, S.; Grugeon, S.; Dupont, L.; Tarascon, J. M. Nano-Sized Transition-Metaloxides as Negative-Electrode Materials for Lithium-Ion Batteries. *Nature* **2000**, *407*, 496–499.
44. Hohenberg, P.; Kohn, W. Inhomogeneous Electron Gas. *Phys. Rev.* **1964**, *136*, B864–B871.
45. Kresse, G.; Furthmuller, J. Efficiency of *Ab Initio* Total Energy Calculations for Metals and Semiconductors Using a Plane-Wave Basis Set. *Comput. Mater. Sci.* **1996**, *6*, 15–50.
46. Kresse, G.; Joubert, D. From Ultrasoft Pseudopotentials to the Projector Augmented-Wave Method. *Phys. Rev. B* **1999**, *59*, 1758–1775.

47. Tasker, P. W. Stability of Ionic-Crystal Surfaces. *J. Phys. C: Solid State Phys.* **1979**, *12*, 4977–4984.
48. Aydinol, M. K.; Kohan, A. F.; Ceder, G.; Cho, K.; Joannopoulos, J. *Ab Initio* Study of Lithium Intercalation in Metal Oxides and Metal Dichalcogenides. *Phys. Rev. B* **1997**, *56*, 1354–1365.
49. Iotova, D.; Kioussis, N.; Lim, S. P. Electronic Structure and Elastic Properties of the Ni_3X (X=Mn, Al, Ga, Si, Ge) Intermetallics. *Phys. Rev. B* **1996**, *54*, 14413–14422.